Multifrequency Interlaced CMUTs for Photoacoustic Imaging

Ryan K. W. Chee, Peiyu Zhang, Mohammad Maadi, and Roger J. Zemp

Abstract—Multifrequency capacitive micromachined ultrasound transducers (CMUTs) are introduced consisting of interlaced 82-μm (low frequency) and 36-μm (high frequency) membranes. The membranes have been interlaced on a scale smaller than the shortest wavelength of operation allowing several advantages over other multifrequency transducer designs including aligned beam profiles, optimal imaging resolution, and minimal grating lobes. The low- and high-frequency CMUTs operate at 1.74 and 5.04 MHz in immersion, respectively. Multifrequency transducers have applications in wideband photoacoustic (PA) imaging where multifrequency transducers are better able to detect both high- and low-frequency PA frequency content. The PA frequency content is target size dependent, which means traditional high-frequency transducers have less sensitivity to larger objects such as diffuse contrast agents. We demonstrate that the low-frequency subarrays are able to better visualize diffuse agent distributions, while the high-frequency subarrays offer fine-resolution imaging important for microvascular imaging and structural navigation. Spectroscopically unmixed images superimpose high sensitivity images of agent concentrations (acquired using low-frequency subarrays) onto high-resolution images of microvessel-mimicking phantoms (acquired using high-frequency subarrays).

Index Terms—Capacitive micromachined ultrasound transducers (CMUTs), multifrequency, photoacoustic (PA) imaging, spectroscopic PA (sPA) imaging.

I. INTRODUCTION

PHOTOACOUSTIC (PA) imaging uses differences in optical absorption to produce high contrast images. PA imaging has the potential for the clinical detection and localization of tumors [1]–[3] and atherosclerotic plaques [4]–[6]. Contrast agents such as dyes and nanoparticles are often used to give added contrast. These contrast agents can be genetically encoded [7]–[9] or injected and molecularly targeted, which result in molecular images that can help to identify and characterize disease. Nanoparticles, for example, can be molecularly targeted to enhance the detection of cancer cells [10]–[13]. In addition, dyes such as indocyanine green can help to enhance tumor contrast to surrounding tissue [14]. Spectroscopic PA (sPA) imaging is the spectral unmixing of PA images of multiple optical wavelengths to quantitatively estimate the concentration of optical absorbers in the body. sPA imaging has been used to image hemoglobin oxygen saturation, total hemoglobin concentration, contrast agent dyes, nanoparticles, and lipid concentrations [4], [15], [16]. Applications include tumor staging in breast cancer [17], lipid monitoring in atherosclerotic plaques [18], and mapping of dye and nanoparticle concentrations [16]. Concentrations of dyes or contrast agents are often only present in diffuse concentrations in the body. PA signals from diffuse concentrations of contrast agents are poorly detected by high-frequency transducers typically used for high resolution PA images. This is in part because the PA signal frequency of an optical absorber is size dependent [19]. Often diffuse distributions of optical dyes or molecularly targeted nanoparticles have slowly varying spatial profiles and will hence produce very low PA frequencies that are difficult to detect with high-frequency transducers used to visualize microvascular networks. Ku *et al.* [20] have demonstrated improved PA images using multiple-bandwidth detection using only single element transducers.

There have been several attempts to develop multifrequency ultrasound array transducers using traditional piezoelectric technology. Stephens *et al.* [21] developed a dual-frequency array transducer consisting of three linear arrays, where the central linear array could be used for high frequency imaging while the outer low-frequency arrays could be used for ultrasound therapy. This design has poor beam alignment and compromised elevational focusing for both imaging and therapy applications, and unaligned beam profiles. Additionally, it is difficult to apply two different acoustic matching layers on the low and high frequency arrays. Azuma *et al.* [22] fabricated a 0.5- and 2-MHz dual layer transducer with a frequency selective isolation layer, but nontrivial acoustic impedance matching was again required. A similar dual layer design featuring 6.5 and 30 MHz has also been recently introduced [23]. Gessner *et al.* [24], [25] demonstrated a dual-frequency (4-MHz transmit and 30-MHz receive) transducer for dual-frequency contrast ultrasound imaging and acoustic angiography, but their system required mechanical scanning and had nonideally coaligned beam profiles. Guiroy *et al.* [26] demonstrated a similar dual-frequency (4-MHz transmit and 14-MHz receive) transducer with curved elements for enhanced sensitivity. None of these prior works has investigated multifrequency arrays for PA applications.

Capacitive micromachined ultrasound transducers (CMUTs) offer several advantages over piezoelectric transducers for multifrequency and PA applications. A number of studies have

demonstrated the use of CMUTs for PA imaging [27]–[30]. CMUTs have excellent PA imaging potential as they exhibit wider bandwidth, easier electronic integration, and less restrictive fabrication allowing for larger arrays, higher frequencies, and new architectures and geometries [27]–[30]. For multifrequency applications, multifrequency CMUTs can be easily impedance matched by matching the radiation impedance to the transmission medium. Less restrictive fabrication greatly simplifies multifrequency transducer fabrication in CMUTs. Thickness and backing define the resonance frequency in piezoelectrics while in CMUTs, for a given membrane thickness this is defined by transducer membrane width which is far easier to vary within an array. Kupnik *et al.* [31] proposed varying CMUT membrane sizes to develop wide bandwidth air coupled transducers for use in range finding and gas flow applications. They showed that it was possible to obtain increased bandwidth operation when membrane sizes were varied in a monotonically increasing radial pattern from the center of the wafer. However, they did not explore multifrequency CMUTs for medical imaging applications. In addition, Bayram *et al.* [32] and Olcum *et al.* [33] have modeled the effect of varying membrane widths on bandwidth improvements and have theoretically shown the potential for bandwidth improvement in both air and immersion operation using this method, but they did not fabricate or test their designs. Eames *et al.* [34], [35] fabricated and modeled CMUTs that could operate at low frequencies in precollapse mode, and then operate at high frequencies by collapsing the top membrane onto a frame to define an effectively smaller membrane size.

Our multifrequency interlaced CMUTs consist of 36-μm (high frequency) and 82-μm (low frequency) cells that have been interlaced on a scale smaller than the smallest operating wavelength. Transducer array elements have been fabricated with a pitch less than the wavelength of the center-operating frequency (the lambda-pitch requirement) resulting in minimal grating lobes. The shortest center-operating wavelength of our high-frequency transducer is 290 μm, while the pitch of our devices can be as little as 235 μm. To the best of our knowledge, no one has taken advantage of the capabilities of CMUTs to be interlaced on a scale smaller than the shortest acoustic wavelength in water/tissue. Our interlaced low- and high-frequency CMUTs will have ideally coaligned beam profiles with optimal imaging resolutions and minimal deleterious grating lobes.

As an extension to our conference proceedings [36], we have fabricated our multifrequency interlaced CMUTs and have demonstrated their application for wide bandwidth PA imaging. We first demonstrate via simulations that PA signal frequency is target size dependent and that our interlaced multifrequency CMUT scheme is ideal for minimal grating lobes. We characterize the resonant frequencies, beam coalignment, and PA lateral resolutions of our devices. Finally, we present sPA images illustrating the ability to better visualize large optical absorber distribution with the low-frequency subarrays while imaging with high resolution with the high-frequency subarrays. We show that the low-frequency subarrays have improved signal-to-noise ratio (SNR) for low-frequency PA content in comparison to the high-frequency subarrays. This paper is the first application of multifrequency CMUT arrays to PA imaging.

II. SIMULATION OF PHOTOACOUSTIC SIGNAL

To illustrate the target size dependence of PA signals, we derive an expression for a 3-D Gaussian diffuse dye distribution and simulate the PA signal at an observation point using MATLAB (Mathworks Inc.). The equations used to simulate the signals are found in [37]. The PA signal at observation field point r due to an arbitrary initial pressure distribution is given as

$$p(r, t) = \frac{1}{4\pi v_s^2} \frac{\partial}{\partial t} \left[\frac{1}{v_s t} \int p_0(r') \delta \left(t - \frac{|r - r'|}{v_s} \right) dr' \right]. \quad (1)$$

Here, $p_0(r) = \Gamma \mu_a(r) \Phi(r)$ models the initial pressure distribution where Γ is the Gruneisen parameter (assumed a constant), μ_a is the optical absorption coefficient distribution, and Φ is the optical fluence. To model a diffuse dye distribution, we consider a weak absorption distribution where the fluence is approximately constant and the absorption distribution is a spherical Gaussian shape. Then

$$\mu_a(r) = \mu_{a0} \exp\left(-\frac{|r - r'|^2}{2\sigma^2} \right). \quad (2)$$

Let the sphere be centered at the origin and the observation point be located a distance r from the center with a standard deviation of σ. To evaluate the PA signal from a diffuse slowly varying distribution at this observation point, we consider spherical shells of infinitesimal thickness with uniform optical absorption. The PA signal from such a shell can be written as the difference between signals from two uniform spheres of radius R_s and $R_s + \Delta R_s$. The signal from a sphere of radius R_s in the following equation can be derived from (1) [37] as:

$$p_{R_s}(r, t) = \frac{r + v_s t}{2r} p_{U, R_S}(r + v_s t) + \frac{r - v_s t}{2r} p_{U, R_S}(-r + v_s t)$$
$$+ \frac{r - v_s t}{2r} p_{U, R_S}(r - v_s t) \quad (3)$$

where

$$p_{U, R_s}(r) = p_i U(r) U(-r + R_S) \quad (4)$$

for $0 \leq r \leq R_S$ and where p_i is the initial pressure and U is the Heaviside step function. We define the signal from a spherical shell with inner and outer radii given as $[R_s, R_s + \Delta R_s]$ as

$$\delta p(r, t) = p_{R_s + \Delta R_s}(r, t) - p_{R_s}(r, t). \quad (5)$$

To obtain the PA signal from a diffuse Gaussian distribution we must substitute $p_0 \exp(-(1/2)(R_s^2/\sigma^2))$ for $p_i(R_s)$ and integrate over spherical shells. This results in the following:

$$p(r, t) = p_0 \left\{ \frac{r + v_s t}{2r} \exp\left(-\frac{1}{2} \frac{(r + v_s t)^2}{\sigma^2} \right) \right.$$
$$\left. + \frac{r - v_s t}{r} \exp\left(-\frac{1}{2} \frac{(r - v_s t)^2}{\sigma^2} \right) \right\}. \quad (6)$$
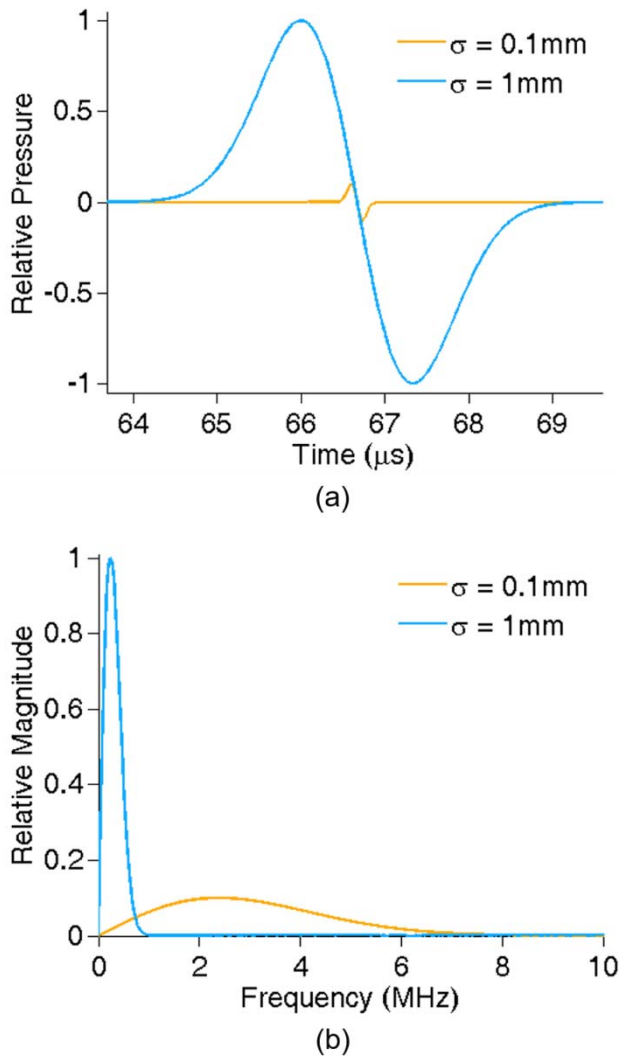
Fig. 1. (a) Simulated PA signals from Gaussian μ_a spatial distributions. (b) Spectrum of PA signals from these distributions. The more slowly varying distribution produces significantly lower frequency content than the more rapidly changing distribution.
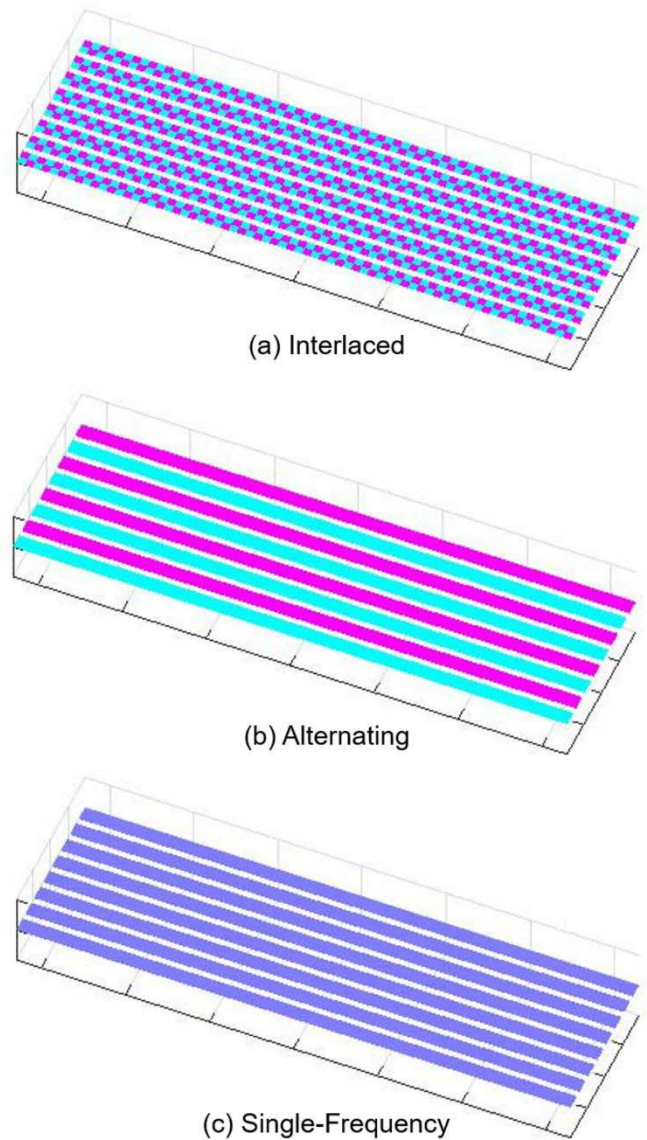

Fig. 2. Simulated transducers (showing only 8 of 99 elements used). (a) Interlaced multifrequency transducer similar to our fabricated devices. (b) Alternating multifrequency transducer. (c) Single-frequency transducer. Blue strips: 1 MHz subelements. Pink strips: 5 MHz subelements.

We can use (6) to plot the PA signal of diffuse dye distributions. Fig. 1(a) shows the simulated PA signals of diffuse dye distributions represented as Gaussian distributions with Gaussian root-mean-square widths, σ, of 0.1 and 1 mm. Fig. 1(b) shows the frequency spectrum of the simulated PA signals of diffuse dye distribution with σ of 0.1 and 1 mm. As expected, the larger optical absorber has significantly lower frequency content than the small optical absorber.

The slowly varying 1-mm distribution spectrum appears lower than would be detectable by many commercial and high-frequency ultrasound transducers. More sharply defined absorption edges may produce more broadband frequency content but this may not always be the case for contrast agents and dyes that have a tendency to diffuse in tissues. Given that many preclinical PA imaging systems use high-frequency transducers to achieve high resolutions, Fig. 1 suggests that such transducers may miss capturing lower frequency signals important for molecular imaging applications. This motivated us to develop multifrequency transducers capable of

high-resolution imaging but also with high sensitivity to diffuse optical distributions.

III. SIMULATED BEAM PROFILES AND PULSE-ECHO POINT SPREAD FUNCTIONS

We considered several multifrequency transducer designs prior to device fabrication. To investigate the issue of grating lobes, we have simulated the acoustic receive point spread functions from several transducer designs. We use Field II in a MATLAB (Mathworks Inc.) environment to perform the simulations [38], [39]. We use three transducers for comparison: an interlaced multifrequency transducer (interlaced), an alternating multifrequency transducer (alternating), and a single-frequency transducer (single frequency). Fig. 2 illustrates the transducers used but includes only 8 of the 99 elements used in the simulation.

Fig. 4. Scanning electron microscope image of interlaced 82- and 36-μm CMUTs.
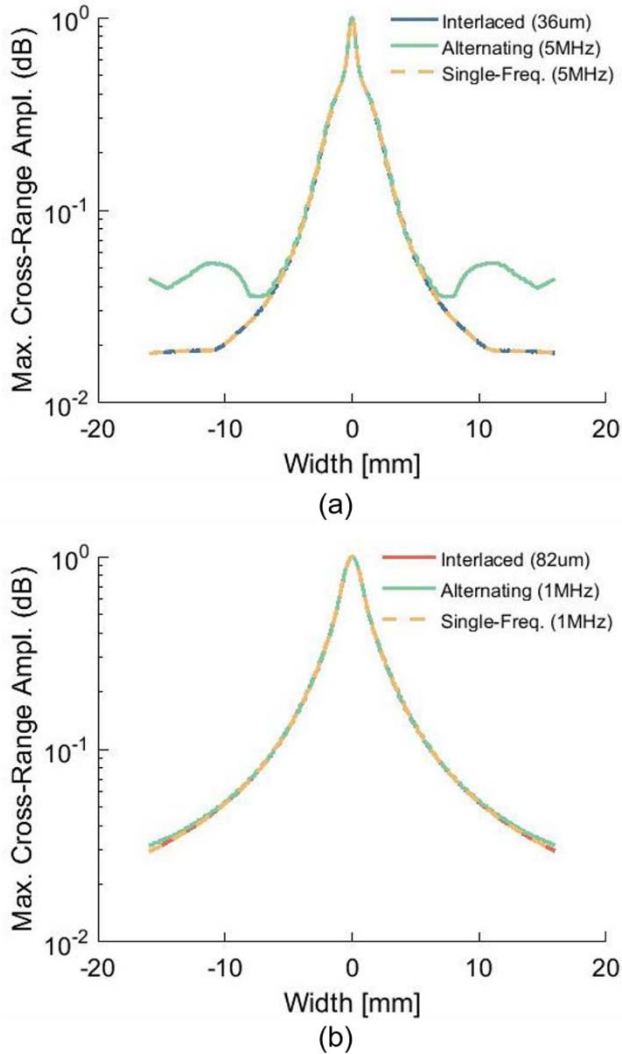
Fig. 3. (a) Comparison of the lateral profiles of the receive point spread functions for different 5-MHz transducers. (b) Comparison of the lateral profiles of the receive point spread functions for different 1-MHz transducers.

The simulated interlaced multifrequency transducer consists of interlaced 1- and 5-MHz devices. The simulated alternating multifrequency transducer consists of alternating 1- and 5-MHz center-frequency elements, and the single-frequency transducers consists of single-frequency elements of either 1- or 5-MHz center frequency. The simulation of the pulse-echo point spread function used 1.5 pulse cycles, 150-MHz sampling frequency, 1450-m/s speed of sound, 99 elements, and device dimensions consistent with the fabricated multifrequency devices (179-μm element width with 250-μm pitch and 6.596-mm height). The receive focus and elevational focusing lens focal length was set to 2 cm above the transducer. A point source was also located at this 2-cm focal position. We obtain the lateral profile of the receive point spread function by finding the maximum value for each lateral position. The lateral profile of the receive point spread function is shown for the interlaced, alternating, and single-frequency transducers operating at 5 and 1 MHz separately.

Fig. 3(a) and (b) shows the comparison of lateral profiles of the receive point spread functions of different transducers
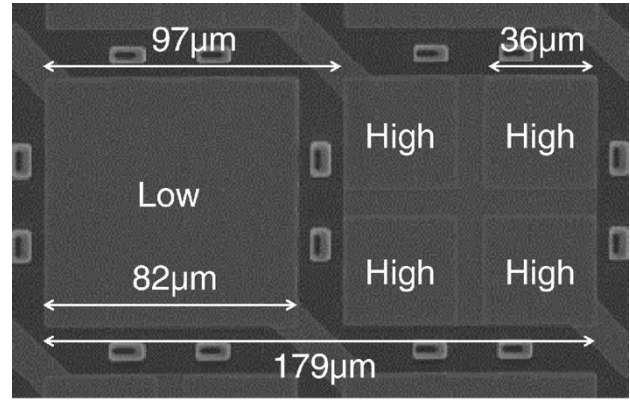
operating at 5 and 1 MHz, respectively. The simulations show that our interlaced transducer has a point spread function similar to the single-frequency transducer, but with the multifrequency functionality. As predicted in theory, the grating lobes can be seen present for the 5-MHz alternating transducer but not the interlaced transducer operating at 5 MHz. The 1-MHz devices have no visible grating lobes. Minimal grating lobes are most important for the high-frequency devices where large grating lobes can cause unwanted imaging artifacts. These results indicate that interlaced CMUTs may be a promising multifrequency transducer architecture.

IV. DEVICE DESIGN AND FABRICATION

We chose center frequencies of 1 MHz (low frequency) and 5 MHz (high frequency) primarily based on the convenience of device geometry. We were able to fit four smaller membranes into roughly the same area as a larger membrane for interlacing as shown in Fig. 4. Multifrequency interlaced CMUTs with a larger difference in center frequencies should be possible in the future work by fitting more membranes of smaller size into the area of the larger interlaced membrane.

We used ANSYS (ANSYS Inc., Canonsburg, PA, USA) to predict the collapse voltages and resonance frequencies of membranes used in our multifrequency devices, as described in our previous conference paper [36]. We designed linear arrays and composite single element transducers consisting of interlaced low- and high-frequency membranes.

We fabricated the multifrequency CMUTs using a standard silicon-nitride sacrificial release process with slight modifications. The process flow is shown in Fig. 5. A heavily boron-doped prime wafer serves as the bottom electrode. Nitride, oxide, and polysilicon are deposited sequentially. The nitride layer acts as a bottom dielectric layer and KOH-etch-stop. The oxide layer acts as an etch-stop layer for the specific inductively coupled plasma deep-reactive ion etching (ICP-DRIE) process used for the nitride layers. Polysilicon serves as a sacrificial layer [Fig. 5(a)]. The polysilicon layer is lithographically patterned to form the etching-channel areas [Fig. 5(b)]. This is followed by another polysilicon deposition [Fig. 5(c)]. This step increases the thickness of the sacrificial polysilicon in the gap area while creating a thin layer of film within the etch-channel that can be
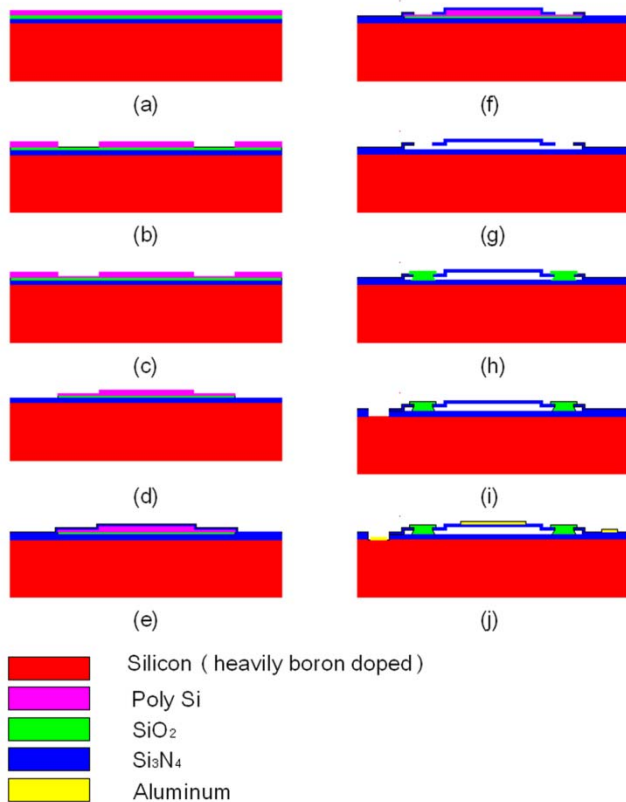
Fig. 5.   Multifrequency sacrificial release fabrication process. (a) A prime wafer with nitride, oxide, polysilicon deposited. (b) Etching-channel is lithographically patterned. (c) Polysilicon is deposited. (d) Pattern polysilicon and oxide layers to define active area. (e) Top membrane is deposited. (f) Sacrificial release hole formed. (g) Membraned released via KOH wet etching. (h) Oxide holes sealed. (i) Access holes to bottom electrode formed. (j) Metalization and patterning of electrodes, interconnects and bond-pads.

Fig. 6.   CMUT layer dimensions.

Fig. 7.   (a) Single element arrays (68×70). (b) Linear arrays (68×2) spaced 235 μm apart to illustrate the scanning arrangement used.

sacrificially removed. Then, the polysilicon and oxide layers are patterned to define the active area (including the cavity and etching channel [Fig. 5(d)]). The next step is the deposition of the top membrane. The top membrane is a "sandwich structure" composed of one layer of stoichiometric silicon nitride, one layer of low-stress (<100 MPa tensile) nitride, and another stoichiometric silicon nitride layer [Fig. 5(e)]. The sandwich structure combines the advantages of ultralow etch-rates of KOH on stoichiometric silicon nitride and the low stresses of the Si_3N_4 membrane material. The higher stress of the thin stoichiometric nitride film contributes negligibly to the overall stress of the membrane. After membrane deposition, a sacrificial release window is formed by ICP-DRIE as shown in Fig. 5(f). KOH wet etching is then used to etch away the polysilicon and oxide and release the membranes [Fig. 5(g)]. Although the etch-rate of oxide is much slower than that of polysilicon, the oxide layer beneath the gap and etch-channel areas will be completely etched away during the long sacrificial etches. In order to seal the cavity and prevent membrane damage, a low-stress Tetraethyl orthosilicate (TEOS) plasma-enhanced chemical vapor deposition (PECVD) oxide film is deposited and patterned to form etch hole sealing plugs. The TEOS oxide offers nonconformal oxide deposition so that etch holes may be sealed without coating the gap area [Fig. 5(h)]. All TEOS oxide is removed from active membrane
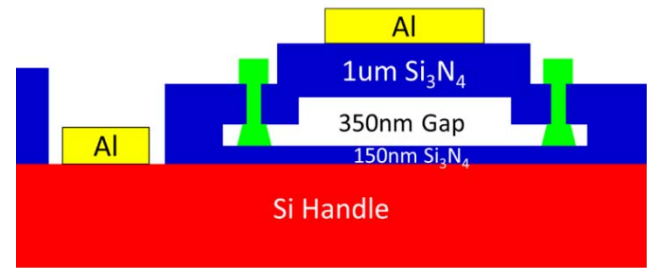
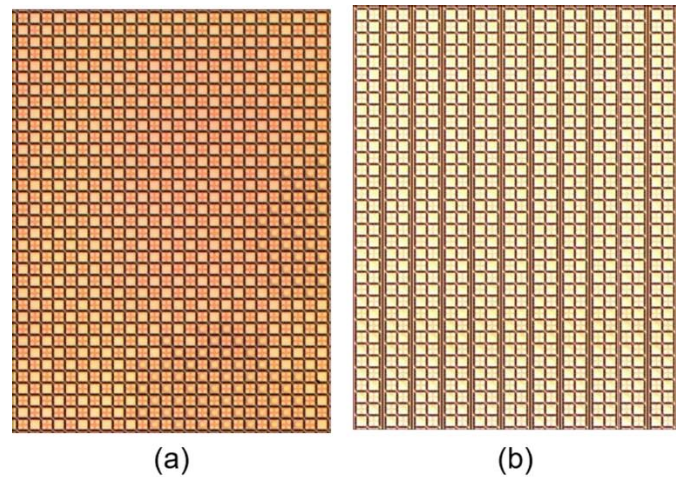areas using buffered oxide etch to ensure no added membrane stress or thickness. The next step is the etching of the nitride layer to form access holes to the bottom electrode [Fig. 5(i)]. Finally, metallization and patterning is performed to form top electrodes, top interconnects, top electrode bond-pads, and the bottom-electrode bond-pads [(Fig. 5(j)]. We coat the final device with Parylene C for electrical isolation and additional hermetic sealing in oil.

We have fabricated 7 mm $\times$ 7 mm dies containing interlaced 82-μm (low frequency) and 36-μm (high frequency) cells. Fig. 6 shows device layer thicknesses.

Two types of arrays were fabricated and tested in our experiments. The first are 7 mm $\times$ 7 mm single-element multifrequency transducers, which have 68×70 connected subelements of alternating 82- and 36-μm cells, as shown in Fig. 7(a). The second are linear array transducers, which have 68×2 connected subelements of alternating 82- and 36-μm cells. Fig. 4 is an example of a 1×2 section. Thus, a 68×2 linear array will have 68 of the 1×2 sections shown in Fig. 4, and they will alternate as shown in Fig. 2(a). A 68×70 single-element array will have 68 rows and 35 columns of the 1×2 sections. In the single-element array, all of the 82-μm cells will be connected together and likewise for the 36-μm cells. Fig. 7(b) is a representation of a scanned linear array as was used in our experiments. The pitch in Fig. 7(b) is 250 μm, which is less than the center-frequency wavelength of the 36-μm membranes in immersion (which is 290 μm) thus maintaining the traditional lambda-pitch requirement for optimal imaging resolution. Each 68×2
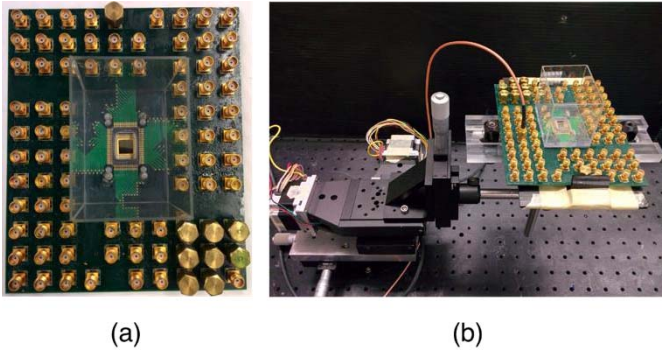
Fig. 8.   (a) Multifrequency CMUT die wirebonded to a CFP80 package and attached to a test fixture with a watertight attachable tank for oil immersion testing. (b) Mechanical scanning setup used for mechanical scanning.
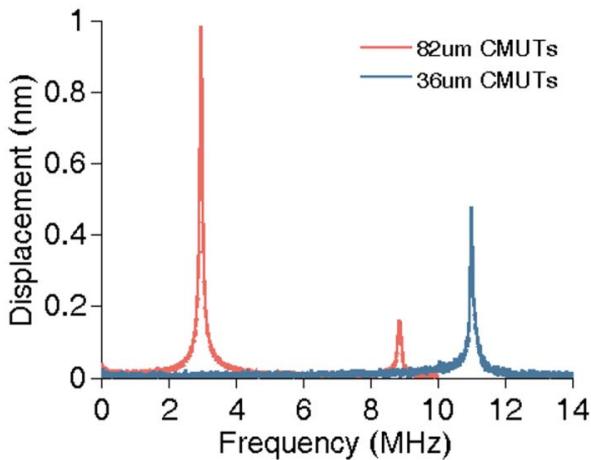

Fig. 10.   (a) Actuation of the 36-μm single element subarrays when driven by a 3-V 11.08-MHz sine wave (+/−60-nm displacement range). (b) Actuation of the 82-μm single element subarrays when driven by a 3-V 2.90-MHz sine wave actuation (+/−80-nm displacement range). Multimedia movies are available.

Fig. 9.   Vibrometer frequency response of 36- and 82-μm single element devices in air.

linear array and 68×70 single element array has two signal and ground bond-pads for driving the 82- and 36-μm membranes separately.

The multifrequency CMUT die was wirebonded to a CFP80 package and attached to a test fixture (CQFP80-SMA Test Fixture, CMC Microsystems) with a watertight attachable tank for oil immersion testing [Fig. 8(a)]. In testing the linear arrays, we mechanically scanned a single 68×2 array over a number of scan positions (n), resulting in a total array size of $68 \times 2n$ [Fig. 7(b) shows a $68 \times 2n$ array where $n = 11$]. Fig. 8(b) shows the mechanical scanning setup.

V. Experiments

A. Actuation in Air—Single Element

We use a vibrometer (MSA-500, Polytec) to image low- and high-frequency cell operations separately in a single element array. We grounded the high-frequency cells while low-frequency cells were operating and vice versa. The 36- and 82-μm devices were biased at 100 and 20 V, respectively. A pseudorandom signal was applied to the 36- and 82-μm devices to determine the center frequency in air. A pseudorandom signal is a signal equally weighted in all frequencies so that a resonance frequency can be detected. Fig. 9 shows the center frequencies of the 36- and 82-μm
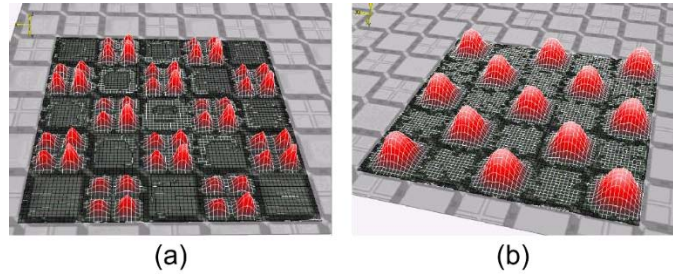
single element cells in air, which were 11.08 and 2.97 MHz, respectively. The 82-μm devices also had a second modal frequency at 8.85 MHz. The observed resonant frequencies of 11.08 and 2.97 MHz in air are close to the simulated 10.5- and 2.1-MHz resonant frequencies in air simulated using ANSYS (ANSYS Inc., Canonsburg, PA, USA) in our previous conference proceedings [36]. The collapse voltages match the simulated values of ∼150 and ∼30 V for the 36- and 82-μm devices, respectively [36].

We obtain device actuation videos by scanning the vibrometer across actuated membranes at a spacing of ∼6.5 μm. We drove the 36- and 82-μm single element subarrays using a 3-V amplitude sine wave at their resonant frequencies.

Fig. 10 shows the device actuation for the 36- and 82-μm single element subarrays. Fig. 10(a) contains the 36-μm single element subarray driven by a 3-V 11.08-MHz sine wave. Fig. 10(b) contains the 82-μm single element subarray driven by a 3-V 2.90-MHz sine wave. Multimedia movies are provided for Fig. 10(a) and (b).

B. Immersion Center Frequency—Single Element Array

We measured the frequency response of the single element multifrequency arrays in oil immersion to characterize its performance in a tissue-like medium. A 7 mm × 7 mm single element die was mounted and wirebonded onto a CFP80 packages. This was then mounted onto a test fixture with attachable tank and filled with vegetable oil. The transmit pressures were detected with a hydrophone (HNP-0400, Onda), and signal was amplified by both a preamp (AH-2010-DCBNS, Onda) and a 39-dB pulser-receiver amplifier (Model 5073PR, Olympus NDT) before being measured by an oscilloscope using 100 times averaging. A pulser-receiver (Model 5900PR, Olympus NDT) was used to supply a short 16 μJ pulse at a 1-kHz pulse repetition rate to the CMUTs. A 20-V bias was applied to the 82-μm devices, and a 100-V bias was applied to the 36-μm devices. Low- and high-frequency devices were tested individually while grounding the nonactive devices.

We found the center frequency of the 82-μm devices in immersion to be 1.74 MHz with a −6-dB bandwidth of 2.33 MHz (Fig. 11). The fractional bandwidth is 134%. The center frequency for the 36-μm devices in immersion was
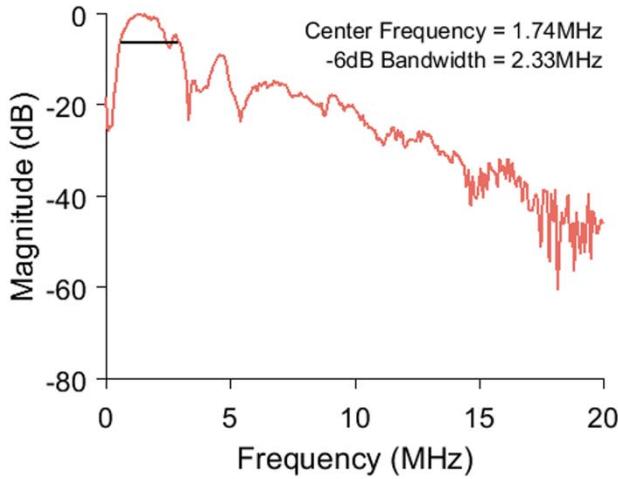
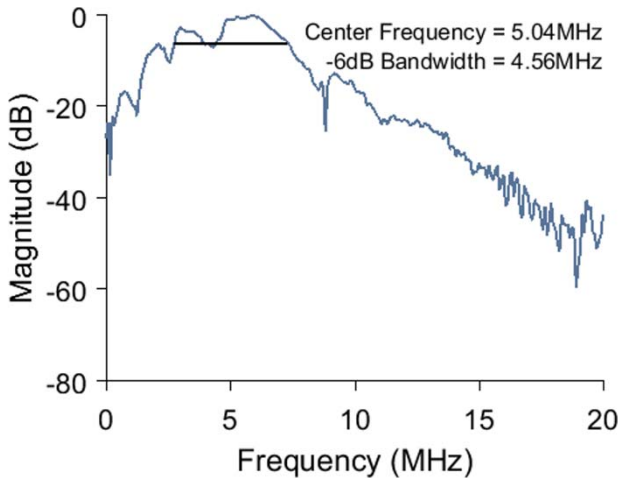Fig. 11.   82-μm frequency response in oil immersion.

Fig. 12.   36-μm frequency response in oil immersion.

5.04 MHz with a −6-dB bandwidth of 4.56 MHz (Fig. 12). The fractional bandwidth is 90%. There is a slight overlap between the high- and low-frequency devices in the 2.76–2.905-MHz range. Our −6-dB sensitivity spans from 0.6 to 7.32 MHz. The effective mean frequency in this range is 3.9 MHz. The best fractional bandwidths reported to date for CMUTs are ~130%. Thus an equivalent 3.9-MHz-center frequency CMUT would only have a bandwidth of 5.1 MHz (spanning 1.4–6.5 MHz). Thus, our multifrequency array offers greater fractional bandwidth (effectively 170% fractional bandwidth) compared to most previous CMUTs using uniformly sized membranes.

We had anticipated a drop in center frequency from our in-air simulation results to immersion testing because immersion operation causes the CMUTs to be heavily damped with a wide bandwidth. The −3-dB bandwidths in immersion for the 82- and 36-μm devices are 1.39 and 3.72 MHz, respectively. The oscillations in the frequency response may be due to substrate ringing modes and/or mutual acoustic interaction. Substrate ringing modes could potentially be avoided by future wafer thinning.
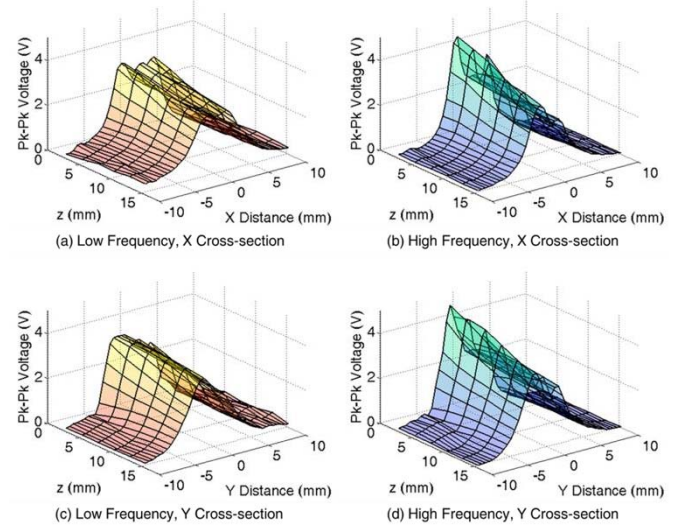

Fig. 13.   (a) Low-frequency (82 μm) beam profile in x-direction. (b) High-frequency (36 μm) beam profile in x-direction. (c) Low-frequency (82 μm) beam profile in y-direction. (d) High-frequency (36 μm) beam profile in y-direction.

C. Beam Profile Coalignment–Single Element Array

We are using 7 mm × 7 mm single element transducers (68 × 70 elements) to justify low- and high-frequency beam coalignment. The transmit beam profiles were studied as a surrogate measure of receive spatial sensitivity coalignment as justified by the principle of reciprocity. We measured the beam profiles along the x- and y-directions in immersion for the low- and high-frequency CMUTs to verify that the beam profiles were coaligned. A 7 mm × 7 mm single element die was mounted and wirebonded onto a CFP80 package. We mounted this onto a test fixture with attachable tank and filled it with vegetable oil. We used a hydrophone (HNP-0400, Onda) to measure the transmit pressures. The CMUTs were driven by a pulser-receiver (Model 5073PR, Olympus NDT). The energy was 4 μJ and the pulse repetition frequency was 1 kHz. The receive signal was amplified by a preamp (AH-2010-DCBNS, Onda) and 54-dB pulser-receiver amplifier (Model 5900PR, Olympus NDT). The receive signals were measured by an oscilloscope using 100 times averaging. The hydrophone was scanned across the x- and y-directions at 0.5-mm increments. This was done for each subarray at five different depths starting at 1 cm away from the transducer surface and increasing by 0.254 cm (0.1 in) to 2.27 cm away. This shows that the beam profiles were coaligned at several depths. The beam profiles are shown in a 3-D graph with the z-axis representing the height of the hydrophone above the multifrequency transducer. x and y represent the positions of the hydrophone along the lateral and elevational directions. The x and y scans for the low- and high-frequency subarrays are shown side-by-side for comparison. The origin is the same for all the scans.

Fig. 13(a) and (b) shows good coalignment between low- and high-frequency beams in the x-direction at all the investigated depths, and Fig. 13(c) and (d) shows good coalignment in the y-direction at all the investigated depths. Some asymmetry is seen in the pressure profiles and is
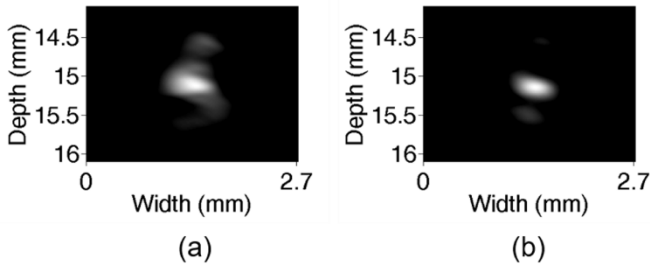
Fig. 14. PA image from (a) 82-μm devices and (b) 36-μm devices.

SNR of Small Hair Target		
Laser λ	Low Frequency	High Frequency
615nm	44.4dB [+3.4dB]	41dB
665nm	42.4dB [+2.3dB]	40.1dB

SNR of Large Methylene Blue Target		
Laser λ	Low Frequency	High Frequency
615nm	52.6dB [+11.8dB]	40.8dB
665nm	52.4dB [+13.1dB]	39.3dB

attributed in part to resistive losses in the bottom electrode. In the future, a higher level of doping will be used.

D. Photoacoustic Imaging

We obtained images using the 82- and 36-μm devices and calculated the lateral resolution. A linear array was scanned linearly to acquire 2-D PA images of a hair. Our target phantom was a human hair immersed in oil. The hair phantom was excited via an Nd:YAG laser (Continuum Surelight III, 10-Hz repetition, $\sim$20 mJ/cm^2). Signal from the array was amplified 40 dB using a pulser-receiver amplifier (Model 5900PR, Olympus NDT) before being acquired by a data acquisition card at a sample rate of 125 MS/s. We biased the 82- and 36-μm devices so that they operated in precollapse mode. We scanned the linear arrays over 93 steps with a step size of 235 μm to create a synthetic aperture of 93 active linear array elements, approximately 6.6 mm $\times$ 21.9 mm in size. The acquired data was then dynamically focused using MATLAB (Mathworks Inc.) to create a 2-D PA image.

Fig. 14(a) and (b) shows a 2-D cross section of a hair obtained using both the 82- and 36-μm devices, respectively. There are sidelobes present in Fig. 14(a) and (b), but they are not visible with the current colormap. We did not use apodization during image reconstruction. We obtain the lateral resolution from the full-width half maximum. The lateral resolution for the 82- and 36-μm devices was 673 and 492 μm, respectively.

The equation for the theoretical lateral resolution is of lateral resolution $\approx 1.4 f_\# \lambda$ where λ is the wavelength and $f_\#$ is the f-number. Using the speed of sound in oil as 1430 m/s and with the active aperture limited to give an $f_\# \sim 1$ during beamforming, the theoretical lateral resolution for the 82- and 36-μm devices is 1151 and 397 μm, respectively. Considering the hair width is $\sim$100 μm, the theoretical lateral resolution for the 36 μm device is comparable to the measured value of 492 μm. For the 82-μm devices, the measured lateral resolution is narrower than the predicted theoretical value. Further device modeling may be required to explain the difference between the theoretical and measured lateral resolutions in the 82-μm devices.

E. Spectroscopic Photoacoustic Imaging

To demonstrate the feasibility of obtaining sPA images of diffuse dye concentrations overlaid on high-resolution images of vasculature, we used two target phantoms, a hair as a small optical absorber mimicking a microvessel and thick dental floss dyed with 0.3% solution of methylene blue (MB) as a

large target mimicking a diffuse optical reporter distribution. The term melanin (MEL) is used interchangeably with hair because MEL is the optical absorber in hair. We immersed the phantoms in oil. The hair was roughly 100 μm in diameter versus the dyed floss, which was roughly 1 mm in diameter. The phantoms were excited via an Nd:YAG laser (Continuum Surelight ND6000, 10-Hz repetition, $\sim$20 mJ/cm^2). Signal from the array was amplified 54 dB before being acquired by a data acquisition card at a sample rate of 125 MS/s. We biased the 82- and 36-μm devices so that they operated in precollapse mode. We scanned the linear arrays over 99 steps with a step size of 250 μm to create a synthetic aperture of 99 active linear array elements, approximately 6.6 mm $\times$ 24.8 mm in size. The acquired data was then dynamically focused using MATLAB (Mathworks Inc.) to create a 2-D PA image. We obtained PA images at optical wavelengths (λ) of 615 and 665 nm. The relative absorption coefficients were found using the peak image intensity of the MB and hair in the 615- and 665-nm images. Spectral demixing was done using MATLAB. The problem is described in detail in [15]. PA intensity is proportional to the absorption coefficient, which is proportional to the sum of extinction coefficient multiplied by concentration. If we take two PA images at different wavelengths, we will have two equations with different values for extinction and absorption coefficients. Given that we have two unknown concentrations, we will be able to solve these equations for the two unknowns.

Table I shows a comparison of the PA SNR of the MEL and MB targets obtained from the low- and high-frequency subarrays at 615- and 665-nm laser wavelengths. We measured the signal amplitude as the average amplitude contained in circular masks that were similar in size to the actual targets. Table I shows that the low-frequency subarrays have higher SNRs for the larger MB target (+12.45-dB average improvement) and the smaller hair target (+2.85-dB average improvement). We indicate the difference in SNR in red. This validates our earlier simulation showing that larger targets have a lower frequency PA signal content. The 12.45-dB
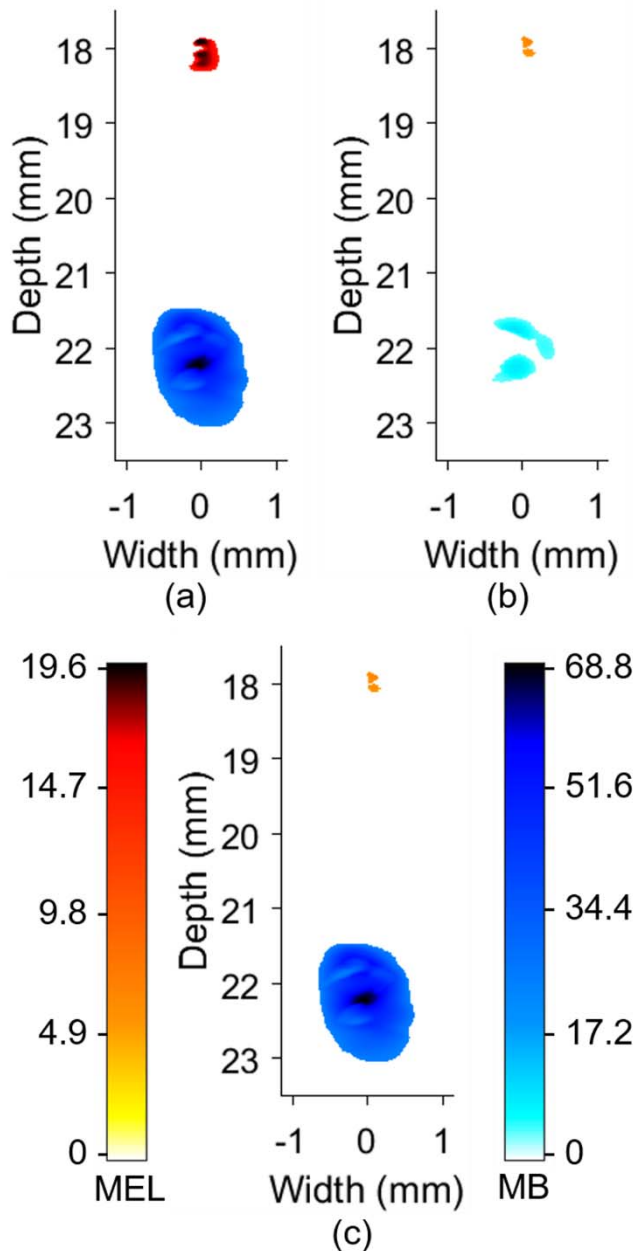
Fig. 15. (a) sPA image of MB and MEL concentration using 82-μm devices (low frequency). (b) sPA image of MB and MEL concentration using 36-μm devices (high frequency). (c) Low-frequency sPA image of MB concentration (higher intensity, lower resolution) overlaid on high-frequency sPA image of MEL concentration (higher resolution). Left: MEL concentration colormap. Right: MB concentration colormap.

improvement in SNR using the low-frequency subarrays is greater than the 6-dB improvement that we would expect using a single-frequency transducer composed of only the high-frequency subarrays.

Fig. 15(a) illustrates the sPA image of MB concentration and MEL concentration using the low-frequency devices. Fig. 15(b) illustrates the sPA image of MB concentration and MEL concentration using the high-frequency devices. Fig. 15(c) shows the low-frequency higher amplitude sPA image of MB concentration overlaid on the high-frequency higher resolution sPA image of MEL concentration (microvessel phantom).

TABLE II
sPA SNR COMPARISON BETWEEN THE LOW-FREQUENCY SUBARRAYS
AND THE HIGH-FREQUENCY SUBARRAYS FOR THE HAIR AND
MB TARGETS. RED INDICATES THE SNR DIFFERENCE

Targets	Low Frequency	High Frequency
MEL	39dB [+9.3dB]	29.7dB
MB	45.3dB [+17.3dB]	28dB

Table II shows a comparison of the sPA SNR of the MEL and MB targets obtained from the low- and high-frequency subarrays. Similar to before, we measured the signal amplitude as the average amplitude contained in circular masks that were similar in size to the actual targets. Table II shows that the low-frequency subarrays have higher SNRs for the larger MB target ($+17.3$-dB improvement) and the smaller hair target ($+9.3$-dB improvement) compared to the high frequency subarrays. We indicate the difference in SNR between the low and high-frequency subarrays in red. The 17.3-dB improvement in SNR using the low-frequency subarrays is greater than the 6-dB improvement that we would expect using a single-frequency transducer composed of only the high-frequency subarrays.

We want to show that having low-frequency subarrays offers the opportunity to better visualize diffuse dye distributions while still being able to produce high-resolution images using the high-frequency subarray. One question is whether the low-frequency subarray offers improved visualization and SNR over the high-frequency subarray for visualizing diffuse dye targets. A second question is whether the low-frequency subarray provides SNR greater than what would be possible with a high-frequency array occupying all the active area of the transducer.

To answer the first question, we compare the SNR of single targets between high- and low-frequency subarrays and show that the low-frequency subarray offers an average of 13.1-dB SNR improvement for 665-nm wavelength illumination over the high-frequency subarray for the larger Methylene blue target. We also do a similar comparison at 615 nm. For these comparisons, the only factor that is changed is whether we use the low- or high-frequency subarray. We also form multiwavelength demixed images and compare the SNR of multiwavelength images between high- and low-frequency subarrays. In this case, we found a 17.3-dB improvement using the low-frequency subarray compared to the high-frequency subarrays. To answer the second question, consider that if the high-frequency subarray were to occupy the whole transducer active area we would anticipate an additional 6-dB improvement in SNR. Our measured low-frequency subarray sensitivities are still greater. Thus, the low-frequency subarrays provide even higher sensitivity to the diffuse dye target than a fully populated high-frequency array.

Note that electromechanical sensitivities and active areas of low- and high-frequency subarrays are designed to be close but may be different, however, this does not matter for the intended purpose. We could add even more active area to the low-frequency devices to improve sensitivity to diffuse dye

distributions at the expense of sensitivity to high-resolution information.

VI. Discussion

The fabrication process used to make these multifrequency devices has the potential for high-throughput manufacturing. This can be accredited to the use of etch-stops for each etching process, high-selectivity sacrificial-release etching, and ICP-DRIE etch-rates as fast as 32 nm/s. Additionally, the interlacing of different-frequency CMUTs is determined simply by the lithography mask design, making this process no more difficult than fabricating single-frequency arrays. This is in sharp contrast with piezoelectric fabrication technology that is limited because of the need to interlace piezoceramics of different thicknesses, which is a great deal harder than fabricating single-frequency arrays.

A potential disadvantage of the interlacing method is the reduced sensitivities of each frequency component. Reduced sensitivity results from the area for each frequency device being halved from sharing real-estate between interlaced low and high frequency elements. There is a potential for nonlinear coupling between low- and high-frequency devices due to mutual acoustic interaction including higher order modes of the low-frequency devices interacting with higher frequency elements and vice versa. In this paper, we read out signal from each subarray one at a time while the other is grounded so electrical crosstalk is principally avoided. Maadi *et al.* [40] has modeled the effect of mutual acoustic impedance between large and small elements for reduced crosstalk.

Section V-E shows the improved wideband detection of both low- and high-frequency PA signal with our multifrequency CMUTs. However, another more direct experiment could have been performed by having a single target type of varying size placed at the same depth location to allow better comparison between detection of low- and high-frequency PA signals with each subarray. The advantage of the experiment we chose to perform is that it more closely simulates a practical application where a diffuse optical dye is present in vasculature.

We have demonstrated that the frequency of PA signals is in part determined by absorber distribution and geometry that may cause problems when trying to image large slowly varying distributions such as diffuse optical dyes in the presence of the surrounding vasculature. While we have focused on using multiband CMUTs for wideband sPA imaging, multifrequency CMUTs would prove equally useful in single-wavelength wideband PA imaging.

In future work, diffuse dye or reporter distributions could be spectroscopically imaged with the low-frequency subaperture for high-sensitivity, and the spectroscopically separated microvasculature and tissue structure could be rendered using data from the high-frequency subaperture.

VII. Conclusion

Our multifrequency interlaced CMUTs consist of interlaced low-frequency (82-μm membrane) and high-frequency (36-μm membrane) cells. We have developed multifrequency interlaced CMUTs with optimal beam coalignment, imaging resolution, and minimal grating lobes by interlacing cells on a scale smaller than the shortest operational wavelength. Our multifrequency interlaced CMUTs are better able to detect wideband PA signal content. We have demonstrated the potential of our multifrequency CMUTs to produce high-resolution images of vasculature using the high-frequency subarrays while better visualizing large slowly varying contrast agent distributions with a higher SNR using the low-frequency subarrays. This work represents the first application of our interlaced multifrequency CMUTs for PA and sPA imaging. Multiband CMUTs may offer a new paradigm for molecular imaging.

References

[1] J. L. Su *et al.*, "Advances in clinical and biomedical applications of photoacoustic imaging," *Expert Opinion Med. Diagnostics*, vol. 4, no. 6, pp. 497–510, Oct. 2010.
[2] V. S. Dogra *et al.*, "Multispectral photoacoustic imaging of prostate cancer: Preliminary *ex-vivo* results," *J. Clin. Imag. Sci.*, vol. 3, no. 41, 2013.
[3] M. Mehrmohammadi, S. J. Yoon, D. Yeager, and S. Y. Emelianov, "Photoacoustic imaging for cancer detection and staging," *Current Molecular Imag.*, vol. 2, no. 1, pp. 89–105, Mar. 2013.
[4] S. Sethuraman, J. H. Amirian, S. H. Litovsky, R. W. Smalling, and S. Y. Emelianov, "Spectroscopic intravascular photoacoustic imaging to differentiate atherosclerotic plaques," *Opt. Exp.*, vol. 16, no. 5, pp. 3362–3367, Mar. 2008.
[5] K. Jansen, A. F. W. van der Steen, H. M. M. van Beusekom, J. W. Oosterhuis, and G. van Soest, "Intravascular photoacoustic imaging of human coronary atherosclerosis," *Opt. Lett.*, vol. 36, no. 5, pp. 597–599, Mar. 2011.
[6] B. Wang *et al.*, "*In vivo* intravascular ultrasound-guided photoacoustic imaging of lipid in plaques using an animal model of atherosclerosis," *Ultrasound Med. Biol.*, vol. 38, no. 12, pp. 2098–2103, 2012.
[7] G. S. Filonov, A. Krumholz, J. Xia, J. Yao, L. V. Wang, and V. V. Verkhusha, "Deep-tissue photoacoustic tomography of a genetically encoded near-infrared fluorescent probe," *Angew. Chem. Int. Ed.*, vol. 51, no. 6, pp. 1448–1451, Feb. 2012.
[8] A. Krumholz, D. M. Shcherbakova, J. Xia, L. V. Wang, and V. V. Verkhusha, "Multicontrast photoacoustic *in vivo* imaging using near-infrared fluorescent proteins," *Sci. Rep.*, vol. 4, Feb. 2014, Art. no. 3939.
[9] L. Li, R. J. Zemp, G. Lungu, G. Stoica, and L. V. Wang, "Photoacoustic imaging of lacZ gene expression *in vivo*," *J. Biomed. Opt.*, vol. 12, no. 2, p. 020504, Apr. 2007.
[10] A. Agarwal *et al.*, "Targeted gold nanorod contrast agent for prostate cancer detection by photoacoustic imaging," *J. Appl. Phys.*, vol. 102, no. 6, p. 064701, Sep. 2007.
[11] S. Mallidi *et al.*, "Multiwavelength photoacoustic imaging and plasmon resonance coupling of gold nanoparticles for selective detection of cancer," *Nano Lett.*, vol. 9, no. 8, pp. 2825–2831, Jul. 2009.
[12] S. Mallidi, T. Larson, J. Aaron, K. Sokolov, and S. Emelianov, "Molecular specific optoacoustic imaging with plasmonic nanoparticles," *Opt. Exp.*, vol. 15, no. 11, pp. 6583–6588, May 2007.
[13] K. A. Homan *et al.*, "Silver nanoplate contrast agents for *in vivo* molecular photoacoustic imaging," *Amer. Chem. Soc. Nano*, vol. 6, no. 1, pp. 641–650, Dec. 2011.

[14] C. Xu *et al.*, "Indocyanine green enhanced co-registered diffuse optical tomography and photoacoustic tomography," *J. Biomed. Opt.*, vol. 18, no. 12, pp. 126006-1–126006-8, Dec. 2013.

[15] B. Cox, J. G. Laufer, S. R. Arridge, and P. C. Beard, "Quantitative spectroscopic photoacoustic imaging: A review," *J. Biomed. Opt.*, vol. 17, no. 6, pp. 061202-1–061202-22, Jun. 2012.

[16] G. P. Luke, S. Y. Nam, and S. Y. Emelianov, "Optical wavelength selection for improved spectroscopic photoacoustic imaging," *Photoacoustics*, vol. 1, no. 2, pp. 36–42, May 2013.

[17] K. E. Wilson, S. V. Bachawal, L. Tian, and J. K. Willmann, "Multiparametric spectroscopic photoacoustic imaging of breast cancer development in a transgenic mouse model," *Theranostics*, vol. 4, no. 11, pp. 1062–1071, 2014.

[18] K. Jansen *et al.*, "Spectroscopic intravascular photoacoustic imaging of lipids in atherosclerosis," *J. Biomed. Opt.*, vol. 19, no. 2, p. 026006, Feb. 2014.

[19] G. J. Diebold, M. I. Khan, and S. M. Park, "Photoacoustic 'signatures' of particulate matter: Optical production of acoustic monopole radiation," *Science*, vol. 250, no. 4977, pp. 101–104, Oct. 1990.

[20] G. Ku, X. Wang, G. Stoica, and L. V. Wang, "Multiple-bandwidth photoacoustic tomography," *Phys. Med. Biol.*, vol. 49, no. 7, pp. 1329–1338, Mar. 2004.

[21] D. N. Stephens, D. E. Kruse, A. S. Ergun, S. Barnes, X. M. Lu, and K. W. Ferrara, "Efficient array design for sonotherapy," *Phys. Med. Biol.*, vol. 53, no. 14, pp. 3943–3969, Jul. 2008.

[22] T. Azuma, M. Ogihara, J. Kubota, A. Sasaki, S.-I. Umemura, and H. Furuhata, "Dual-frequency ultrasound imaging and therapeutic bilaminar array using frequency selective isolation layer," *IEEE Trans. Ultrason., Ferroelect., Freq. Control*, vol. 57, no. 5, pp. 1211–1224, May 2010.

[23] J. Ma, K. H. Martin, P. A. Dayton, and X. Jiang, "A preliminary engineering design of intravascular dual-frequency transducers for contrast-enhanced acoustic angiography and molecular imaging," *IEEE Trans. Ultrason., Ferroelect., Freq. Control*, vol. 61, no. 5, pp. 870–880, May 2014.

[24] R. C. Gessner, C. B. Frederick, F. S. Foster, and P. A. Dayton, "Acoustic angiography: A new imaging modality for assessing microvasculature architecture," *J. Biomed. Imag.*, vol. 2013, no. 14, Jan. 2013.

[25] R. Gessner, M. Lukacs, M. Lee, E. Cherin, F. S. Foster, and P. A. Dayton, "High-resolution, high-contrast ultrasound imaging using a prototype dual-frequency transducer: *In vitro* and *in vivo* studies," *IEEE Trans. Ultrason., Ferroelect., Freq. Control*, vol. 57, no. 8, pp. 1772–1781, Aug. 2010.

[26] A. Guiroy *et al.*, "Dual-frequency transducer for nonlinear contrast agent imaging," *IEEE Trans. Ultrason., Ferroelect., Freq. Control*, vol. 60, no. 12, pp. 2634–2644, Dec. 2013.

[27] S. Vaithilingam *et al.*, "Three-dimensional photoacoustic imaging using a two-dimensional CMUT array," *IEEE Trans. Ultrason., Ferroelect., Freq. Control*, vol. 56, no. 11, pp. 2411–2419, Nov. 2009.

[28] S. Kothapalli, T.-J. Ma, S. Vaithilingam, O. Oralkan, B. T. Khuri-Yakub, and S. Sam Gambhir, "Deep tissue photoacoustic imaging using a miniaturized 2-D capacitive micromachined ultrasonic transducer array," *IEEE Trans. Biomed. Eng.*, vol. 59, no. 5, pp. 1199–1204, May 2012.

[29] R. K. W. Chee, A. Sampaleanu, D. Rishi, and R. J. Zemp, "Top orthogonal to bottom electrode (TOBE) 2-D CMUT arrays for 3-D photoacoustic imaging," *IEEE Trans. Ultrason., Ferroelect., Freq. Control*, vol. 61, no. 8, pp. 1393–1395, Aug. 2014.

[30] X. Cheng, J. Chen, and C. Li, "A miniature capacitive micromachined ultrasonic transducer array for minimally invasive photoacoustic imaging," *J. Microelectromech. Syst.*, vol. 19, no. 4, pp. 1002–1011, Aug. 2010.

[31] M. Kupnik, M.-C. Ho, S. Vaithilingam, and B. T. Khuri-Yakub, "CMUTs for air coupled ultrasound with improved bandwidth," in *Proc. IEEE Int. Ultrason. Symp. (IUS)*, Oct. 2011, pp. 592–595.

[32] C. Bayram, S. Olcum, M. N. Senlik, and A. Atalar, "Bandwidth improvement in a cMUT array with mixed sized elements," in *Proc. IEEE Ultrason. Symp.*, vol. 4. Sep. 2005, pp. 1956–1959.

[33] S. Olcum, A. Atalar, H. Koymen, and M. N. Senlik, "P3R-4 stagger tuned cMUT array for wideband airborne applications," in *Proc. IEEE Ultrason. Symp.*, Oct. 2006, pp. 2377–2380.

[34] M. D. C. Eames, T. J. Reck, and J. A. Hossack, "Selectable frequency CMUT with membrane stand-off structures," in *Proc. IEEE Int. Ultrason. Symp. (IUS)*, Sep. 2009, pp. 2814–2817.

[35] M. D. C. Eames, T. J. Reck, J. P. Kilroy, and J. A. Hossack, "FEA modeling of CMUT with membrane stand-off structures to enable selectable frequency-mode operation," *IEEE Trans. Ultrason., Ferroelect., Freq. Control*, vol. 58, no. 12, pp. 2749–2752, Dec. 2011.

[36] P. Zhang, W. Zheng, W. Moussa, and R. J. Zemp, "CMUTs with interlaced high- and low-frequency elements," in *Proc. IEEE Int. Ultrason. Symp. (IUS)*, Oct. 2011, pp. 116–119.

[37] L. V. Wang and H.-I. Wu, "Photoacoustic tomography," in *Biomedical Optics: Principles and Imaging*, 1st ed. Hoboken, NJ, USA: Wiley, 2007, ch. 12, sec. 5, pp. 288–290.

[38] J. A. Jensen, "Field: A program for simulating ultrasound systems," presented at the 10th Nordic-Baltic Conf. Biomed. Imag. Pub. Med. Biol. Eng. Comput., vol. 34. 1996, pp. 351–353.

[39] J. A. Jensen and N. B. Svendsen, "Calculation of pressure fields from arbitrarily shaped, apodized, and excited ultrasound transducers," *IEEE Trans. Ultrason., Ferroelect., Freq. Control*, vol. 39, no. 2, pp. 262–267, Mar. 1992.

[40] M. Maadi and R. J. Zemp, "Self and mutual radiation impedances for modeling of multi-frequency CMUT arrays," *IEEE Trans. Ultrason., Ferroelect., Freq. Control*, vol. 63, no. 9, pp. 1441–1454, Sep. 2016.

Ryan K. W. Chee received the B.Sc. degree in electrical engineering from the University of Alberta, Edmonton, AB, Canada, where he is currently pursuing the Ph.D. degree with the Electrical and Computer Engineering Department.

His current research interests include photoacoustic imaging, capacitive micromachined ultrasonic transducers, and biomedical imaging.

Peiyu Zhang received the B.S. degree from the Zhengzhou Institute of Technology, Zhengzhou, China, the M.S. degree from the Harbin Institute of Technology, Harbin, China, and the Ph.D. degree from Tsinghua University, Beijing, China.

He was a Postdoctoral Fellow with the Institute of Microelectronics, Peking University, Beijing, and the Department of Electrical and Computer Engineering, University of Calgary, Calgary, AB, Canada. He was a Postdoctoral Research Fellow with the University of Alberta, Edmonton, AB. His current research interests include biomedical microelectromechanical systems (MEMS), optical MEMS, and capacitive micromachined ultrasonic transducers.

Mohammad Maadi was born in Macoo, Iran, in 1985. He received the M.S. degree in electrical and electronics engineering from Middle East Technical University (METU), Ankara, Turkey, in 2013. He is currently pursuing the Ph.D. degree with the Electrical and Computer Engineering Department, University of Alberta, Edmonton, AB, Canada.

He was a Research Assistant with METU from 2011 to 2013, where he was involved in the integrated circuit design for capacitive micromachined ultrasonic transducers (CMUTs). He is currently a Research and Teaching Assistant with the University of Alberta. His current research interests include the design, fabrication, and characterization of multifrequency CMUT arrays with associated electronics for ultrasound contrast agent imaging applications.

Mr. Maadi is a member of the Golden Key International Society, the world's largest collegiate honor society. In 2016, he was a recipient of the Alberta Innovates Technology Futures Graduate Student Scholarship.

Roger J. Zemp was born in Calgary, AB, Canada, in 1974. He received the B.Sc. degree in physics from the University of Alberta, Edmonton, AB, in 1998, the M.A.Sc. degree in electrical and computer engineering from the University of Toronto, Toronto, ON, Canada, in 2000, and the Ph.D. degree in biomedical engineering from the University of California at Davis, Davis, CA, USA, in 2004.

He was a Postdoctoral Fellow with Texas A&M University, College Station, TX, USA, from 2004 to 2006, and with Washington University, St. Louis, MO, USA, from 2006 to 2007. He is currently an Associate Professor with the Department of Electrical and Computer Engineering, University of Alberta. His current research interests include ultrasound imaging, biomedical optics, and photoacoustic imaging.